MOX-Report No. 62/2017

A Transmurally Heterogeneous Orthotropic Activation Model for Ventricular Contraction and its Numerical Validation

Barbarotta, L.; Rossi, S.; Dede', L.; Quarteroni, A.

MOX, Dipartimento di Matematica
Politecnico di Milano, Via Bonardi 9 - 20133 Milano (Italy)

mox-dmat@polimi.it http://mox.polimi.it

Received date; | Revised date; | Accepted date

DOI: xxx/xxxx

A Transmurally Heterogeneous Orthotropic Activation Model for Ventricular Contraction and its Numerical Validation

L. Barbarotta*[1] | S. Rossi[2] | L. Dedè[3] | A. Quarteroni[3,4]

[1]Department of Biomedical Engineering, Technische Universiteit Eindhoven, Netherlands
[2]Department of Mathematics, University of North Carolina, NC, USA
[3]Dipartimento di Matematica, Politecnico di Milano, Italy
[4]Institute of Mathematics, Ecóle Polytechnique Fédérale de Lausanne, Switzerland

Correspondence
*L. Barbarotta, Department of Biomedical Engineering, Technische Universiteit Eindhoven, PO Box 513, 5600 MB, Eindhoven, Netherlands.
Email: l.barbarotta@tue.nl

Abstract

Models for cardiac mechanics require an activation mechanism properly representing the stress-strain relations in the contracting myocardium. In this paper, we propose a new activation model which accounts for the transmural heterogeneities observed in myocardial strain measurements. In order to take into account the anisotropy of the active mechanics, our model is based on an active strain formulation. Thanks to its multiplicative decomposition of the deformation gradient tensor, in this formulation the active strains orthogonal to the fibers can be naturally described. We compare the results of our novel orthotropic formulation against different anisotropic models of the active contraction of the cardiac muscle and, moreover, against experimental data available in the literature. We show that the currently available models can represent only some global quantities, but the strain distributions are not in agreement with the reported experimental measurements. Conversely, we show that our new transmurally heterogeneous orthotropic activation model improves the accuracy of shear strains related to in-plane rotations and torsion.

KEYWORDS:
Cardiac Mechanics, Active Strain Formulation, Finite Element Method, Transmurally Heterogeneous Orthotropic Activation

1 | INTRODUCTION

From a mathematical perspective, the contraction of the heart is a complex multiphysics and multiscale process[1]. An electric signal spreads through the muscle, initiating subcellular chemical reactions and thus leading to cellular shortening. The synchronous shortening of the cardiac cells generates muscle contraction which results in the ejection of blood from the atria to the ventricles and from the ventricles to pulmonary and systemic circulations. Any dysfunction in this sequence of events may lead to fatal consequences.[1]

Computational models can significantly help to increase the understanding of the heart function and disfunction. As the computing power increases, electro-mechanical and electro-fluid-mechanical models of the heart have been developed and numerically resolved[3,4,5,6,7,8,1,9,10]. Unfortunately, it is still unclear what are the limitations and the real predictive capabilities of such models. In fact, many models fail in capturing the most obvious characteristics of the heart deformation. The left ventricular apex-to-base shortening, due to the downward motion of the aortic valve ring during systole, is the most important feature of cardiac contraction, indeed allowing the heart to work efficiently. Such deformation is often missing even in recent heart models[11]. In some instances, the models may even lead toward the opposite behavior of what expected, thus resulting in apex-to-base lengthening and unrealistic rotations[12]. It is hence clear that the mathematical modeling of the active contraction of the heart is particularly challenging. Since the ventricular pressure-volume relations can be captured even

[1]In the United States of America only the lifetime risk of developing heart failure is 20% for people over the age of 40, with a 50% rate of mortality within 5 years of diagnosis[2].

in models where the ventricular wall motion is not accurately represented, the validation of the mathematical formulation requires a more in-depth comparison of the myocardial wall strains with respect to experiments.

Since the computational cost of multiphysics computational models is very large, new and enhanced mathematical descriptions of the cardiac contraction can be achieved more easily by isolating the dominating underlying phenomena with respect to the outputs of interest. Hence, in this work suitable assumptions are made to decouple the mechanical deformation of the ventricle from the fluid dynamics and from the electrophysiology. The influence of blood flow is accounted for by means of pressure boundary conditions, the electrical activation is assumed to be uniform in space and the microscopic forces generated by the subcellular crossbridge dynamics are replaced with an explicit time-dependent function.

Typical models of passive mechanics are based on a hyperelastic description for the elastic behavior: the stress-strain relationship can be derived from the Helmholtz free energy characterizing the system. The myocardium is typically considered as an orthotropic material [13] or as a transversely isotropic material [14]. For the active contraction two different approaches are commonly used: the active stress [15,14,16,17] approach and the active strain approach [18,19,20]. The former is based on an additive decomposition of the stress tensor into passive and active components, the latter instead on a multiplicative decomposition of the deformation gradient tensor. Actually, a formulation where the stress is additively decomposed into passive and active components can also be obtained by using a multiplicative decomposition of the deformation gradient tensor [21,22]. In this sense, an active stress formulation can be obtained using an active strain approach. For historical reasons, we denote as active stress formulations only those approaches where the decomposition of the deformation gradient tensor is not considered. Conversely, we denote as active strain formulations the approaches where the multiplicative decomposition of the deformation gradient tensor is applied to the whole free energy. These approaches to model the active contraction of the ventricular muscle can be derived from thermodynamical principles [20] by postulating a special form of the free energy density function. In particular, it is assumed that the free energy depends on the deformation gradient tensor and on some internal variables describing the active state of the muscle. In the active stress models, the active component of the free energy is typically a function of a scalar internal variable, usually representing the biochemical reactions that lead to cellular contraction [20]. In the active strain models, the internal variable describing muscular contraction is the active part of the deformation gradient tensor.

The amount of contraction in the left ventricle varies along the transmural direction: on the endocardium, the inner surface of the heart, the myocardium shortens in cross-fiber direction of about 25%, while on the epicardium, the outer surface of the heart, this shortening is less than 5% [23]. Mathematical models of the active myocardium usually neglect this transmural variation. In this work, we propose a novel transmurally heterogeneous orthotropic model based on an active strain formulation. The use of the active strain formulation allows us to easily describe the anisotropic behavior of cardiac contraction. We compare the new model with experimental data and measurements, a recent active stress formulation [17] and other active strain models [19,24]. In particular, in the comparison we consider other anisotropic active models, such as the transversely isotropic active strain model [25,19] and the orthotropic activation model [20].

In our computational model, which employs spatial approximation based on the finite element method [26], the equilibrium configuration of the system is described by the quasi-static formulation of the momentum equation. The constraint of incompressibility of the cardiac tissue is enforced using a penalty method, postulating the existence of a volumetric energy with a large bulk modulus [27]. To reduce volumetric locking in the displacement-based formulation of the problem, we use a high-order finite element discretization of the quasi-static problem [28]. In particular, we employ quadratic basis functions on simplex elements.

The paper is structured as follows. In Section 2 we introduce the models of the passive mechanics of the left ventricle. In particular, after recalling some notions of finite elasticity, we describe our choice of the constitutive model; we also describe the approach used to enforce the incompressibility constraint. In Section 3, we introduce the active strain approach and some of its variants. In Section 4, we derive the weak formulation of the quasi-static elasticity problem and we describe the finite element formulation and the Newton method used to solve the nonlinear problem. In Section 5, we show the numerical results. We analyze the influence of the boundary conditions on the solution and we compare our results against experimental measurements. By using this analysis, we select suitable boundary conditions for the comparison of the different activation models described in Section 3. By comparing again the numerical results with respect to experimental data at systole, we analyze which models better describe the ventricular contraction. We conclude in Section 6 by providing some perspective on the work done.

2 | PASSIVE CARDIAC MECHANICS

In this section, we formulate the passive mechanical problem. We explain the assumptions at the basis of our formulation and we describe the constitutive model.

FIGURE 1 Idealized left ventricular geometry with boundaries $\Gamma_{0,D}, \Gamma_{0,N}, \Gamma_{0,R}$ highlighted in different colors to distinguish the three subsets of $\partial\Omega_0$ on which we set the boundary conditions (Dirichlet, Natural and Robin, respectively).

2.1 | Notion of Continuum Mechanics

For a deforming body of material, we denote with Ω_0 and Ω the initial and current configurations, respectively. In particular, we take Ω_0 and Ω to be two open sets in $\mathbf{R}^3$ with Lipschitz boundaries. The deformation is characterized by the motion $\boldsymbol{\phi}: \Omega_0 \to \Omega$ such that $\mathbf{x} = \boldsymbol{\phi}(\mathbf{x}_0)$, which maps the reference coordinate $\mathbf{x}_0 \in \Omega_0$ to the current one $\mathbf{x} \in \Omega$. The vector $\mathbf{u} = \mathbf{x} - \mathbf{x}_0$ represents the displacement field and relates the position of a particle in the reference configuration $\mathbf{x}_0$ to its position in the current configuration $\mathbf{x}$. We denote the boundaries of Ω_0 and Ω as $\Gamma_0 = \partial\Omega_0$ and $\Gamma = \partial\Omega$, respectively. We also assume that $\boldsymbol{\phi}$ is a diffeomorphism from Ω_0 to Ω, such that the deformation gradient tensor $\mathbf{F} = \nabla\mathbf{x} = \mathbf{I} + \nabla\mathbf{u}$ and the deformation Jacobian determinant $J = \det(\mathbf{F}) > 0$ are always well defined. We denote with $\mathbf{H} = J\mathbf{F}^{-T}$ the cofactor of the tensor $\mathbf{F}$.

The equations of Lagrangian solid dynamics describe the rate of change of position, density, and momentum of a material body, and can be expressed in an inertial reference frame. In the reference configuration, the equation of static equilibrium are expressed as

$$\rho J = \rho_0 \qquad \text{in } \Omega_0, \tag{1a}$$

$$-\nabla_0 \cdot \mathbf{P} = \rho_0 \mathbf{b} \qquad \text{in } \Omega_0, \tag{1b}$$

where ρ_0 and ρ are the reference and current densities, $\mathbf{P}\left(\mathbf{F}\left(\mathbf{x}_0\right)\right)$ is the first Piola-Kirchhoff stress tensor, $\nabla_0 \cdot$ is the divergence operator with respect to the reference coordinates and $\mathbf{b}$ represents the external forces acting on the body. In the theory of hyperelasticity, $\mathbf{P}$ is obtained from a strain energy function $\mathcal{W}(\mathbf{C})$ as

$$\mathbf{P} = \frac{\partial \mathcal{W}}{\partial \mathbf{C}} \frac{\partial \mathbf{C}}{\partial \mathbf{F}}, \quad \mathbf{C} = \mathbf{F}^T\mathbf{F}, \tag{2}$$

where $\mathbf{C}$ is the right Cauchy-Green deformation tensor. In the following, we will assume $\mathbf{b} = \mathbf{0}$, since the external forces are negligible compared to the internal forces. Equation (1b) needs to be supplied with appropriate boundary conditions, with this aim, we split the boundary of the left ventricle into three subsets $\Gamma_{0,D}$, $\Gamma_{0,N}$ and $\Gamma_{0,R}$, such that $\partial\Omega_0 = \Gamma_{0,D} \cup \Gamma_{0,N} \cup \Gamma_{0,R}$. These are shown in Fig. 1 . $\Gamma_{0,D}$ represents the left ventricular basal plane, where we typically impose a Dirichlet condition to anchor the ventricle in order to avoid rigid displacements and rotations. Different choices are possible, such as preventing any displacement and rotation in the whole basal plane or preventing motion in the innermost region of the basal ring. Our choice is to constrain only the motion along the direction normal to the basal surface.

The surface region $\Gamma_{0,R}$ indicates the epicardium, the outmost external surface of the myocardium. Here, to represent the interaction between the ventricle and the adherent tissues, we set a Robin condition which introduces a linear relation between displacement and stress:

$$\mathbf{P}\mathbf{N}_0 = -\mathbf{A}\mathbf{u} + \boldsymbol{\beta} \quad \text{on } \Gamma_{0,R}, \tag{3}$$

where $\mathbf{A}$ is a second order tensor representing the stiffness of adherent tissues, $\boldsymbol{\beta}$ a stress vector and $\mathbf{N}_0$ is the outward direction unit vector normal to the reference surface Γ_0. Note that, by setting both $\mathbf{A}$ and $\boldsymbol{\beta}$ to zero we obtain the usual stress free condition. By taking $\boldsymbol{\beta} = \mathbf{0}$ and $\mathbf{A} = \alpha\mathbf{I}$, we look for a suitable value for the coefficient α in order to provide a physically meaningful representation of the cardiac contraction. A positive value of α introduces a stiffness that prevents rigid body translations and rotations.

Finally, the surface region $\Gamma_{0,N}$ represents the endocardium, the inner part of the myocardium where the muscle is in contact with the blood flow inside the ventricular cavity. On this subset of the boundary, we set a natural boundary condition to describe the force that the blood exerts on the ventricular wall. We assume that the ventricular pressure in the cavity p_v is uniformly distributed and that the stress is directed along the normal of the deformed surface. Since the deformed configuration is unknown, we resort to the Piola transformation, which

is nonlinear, in order to reformulate the boundary condition in the known reference configuration:

$$\mathbf{P}\mathbf{N}_0 = -p_v \mathbf{H}\mathbf{N}_0 \qquad \text{on } \Gamma_{0,N}. \tag{4}$$

In summary, the final problem in its strong formulation, endowed with boundary conditions, reads:

$$-\nabla_0 \cdot \mathbf{P}(\mathbf{u}) = \mathbf{0} \qquad \text{in } \Omega_0 \tag{5a}$$
$$\mathbf{u} \cdot \mathbf{N}_0 = \mathbf{0} \qquad \text{on } \Gamma_{0,D} \tag{5b}$$
$$\left(\mathbf{I} - \mathbf{N}_0 \otimes \mathbf{N}_0\right)\mathbf{P}\mathbf{N}_0 = \mathbf{0} \qquad \text{on } \Gamma_{0,D} \tag{5c}$$
$$\mathbf{P}\mathbf{N}_0 = -p_v \mathbf{H}\mathbf{N}_0 \qquad \text{on } \Gamma_{0,N} \tag{5d}$$
$$\mathbf{P}\mathbf{N}_0 = -\alpha \mathbf{u} \qquad \text{on } \Gamma_{0,R}. \tag{5e}$$

All equations depend on the time $t > 0$. Note that we omitted (1a) in (5) because incompressibility will be weakly enforced using a nearly incompressible formulation (see section 2.3). By introducing the Hilbert space

$$V = \left\{ \mathbf{v} \in [H^1(\Omega_0)]^3 \,:\, \mathbf{v} \cdot \mathbf{N}_0 = 0 \quad \text{on } \Gamma_{0,D} \right\}, \tag{6}$$

the weak formulation of problem (5) reads: find $\mathbf{u} \in V$ such that

$$\int_{\Omega_0} \mathbf{P}(\mathbf{u}) \,:\, \nabla_0 \mathbf{v} \mathrm{d}\mathbf{V} + \int_{\Gamma_{0,N}} p_v J \mathbf{F}^{-T} \mathbf{N}_0 \cdot \mathbf{v} \mathrm{d}\mathbf{A} + \int_{\Gamma_{0,R}} \alpha \mathbf{u} \cdot \mathbf{v} \mathrm{d}\mathbf{A} = 0 \quad \forall \mathbf{v} \in V. \tag{7}$$

The choice of the functional space is made compatibly with the need to compute gradient of $\mathbf{v}$ and $\mathbf{u}$ and to preserve square integrability in the sense of Lebesgue.

2.2 | Constitutive law

We still need to characterize, in problem (7), the form of the stress tensor. It is common to assume that the myocardial tissue is a hyperlestic material [14,29,13,30] for which the stress tensor can be derived from a pseudo strain-energy function, that representing cardiac tissue needs to account for the microstructural composition of the tissue, in which collagen sheets separate bundles of cardiac cells [31]. We denote with $\mathbf{f}_0$ and $\mathbf{s}_0$ the orientation of the cardiac fibers and collagen sheets respectively, and we assume that these two fields are mutually orthogonal, i.e. $\mathbf{f}_0 \cdot \mathbf{s}_0 = 0$. We create a local orthonormal frame of reference by introducing the cross-fiber field (normal to the collagen sheets) $\mathbf{n}_0 = \mathbf{f}_0 \times \mathbf{s}_0$. The orthonormal frame defined by the vectors $(\mathbf{f}_0, \mathbf{s}_0, \mathbf{n}_0)$ is local as it follows the complex arrangement of the cardiac cells throughout the tissue. The vectors $\mathbf{f}$, $\mathbf{s}$ and $\mathbf{n}$ denote the deformed preferential directions $\mathbf{F}\mathbf{f}_0$, $\mathbf{F}\mathbf{s}_0$ and $\mathbf{F}\mathbf{n}_0$, resepctively. With the above assumptions it is natural to consider the myocardial tissue as orthotropic, that is the mechanical response of the tissue is different along the three mutually orthogonal direction $(\mathbf{f}_0, \mathbf{s}_0, \mathbf{n}_0)$. In this paper, we consider all these material properties by using the constitutive law proposed by Holzapfel and Ogden [13].

To guarantee frame indifference, the strain-energy function is defined as a function of the invariants of the right Cauchy-Green strain tensor $\mathbf{C} = \mathbf{F}^T\mathbf{F}$. In particular, the Holzapfel-Ogden constitutive law [32] additively decomposes the soft isotropic mechanical response of the extracellular matrix and the stiff mechanical behavior of the fibers. By introducing the isotropic invariants

$$\mathcal{I}_1(\mathbf{C}) = \mathrm{tr}\,\mathbf{C}, \quad \mathcal{I}_3(\mathbf{C}) = \det \mathbf{C} \tag{8}$$

and the anisotropic invariants

$$\mathcal{I}_{4,\mathrm{f}}(\mathbf{C}) = \mathbf{f}_0 \cdot \mathbf{C}\mathbf{f}_0, \quad \mathcal{I}_{4,\mathrm{s}}(\mathbf{C}) = \mathbf{s}_0 \cdot \mathbf{C}\mathbf{s}_0, \quad \mathcal{I}_{8,\mathrm{fs}}(\mathbf{C}) = \mathbf{f}_0 \cdot \mathbf{C}\mathbf{s}_0, \tag{9}$$

this model is the sum of four independent terms

$$\mathcal{W}(\mathbf{C}) = \mathcal{W}(\mathcal{I}_1, \mathcal{I}_{4,\mathrm{f}}, \mathcal{I}_{4,\mathrm{s}}, \mathcal{I}_{8,\mathrm{fs}}) = \mathcal{W}_1(\mathcal{I}_1) + \mathcal{W}_{4,f}(\mathcal{I}_{4,\mathrm{f}}) + \mathcal{W}_{4,s}(\mathcal{I}_{4,\mathrm{s}}) + \mathcal{W}_{8,fs}(\mathcal{I}_{8,\mathrm{fs}}), \tag{10}$$

each component being of exponential-type,

$$\begin{aligned}
\mathcal{W}_1(\mathcal{I}_1) &= \frac{a}{2b}\left(e^{b(\mathcal{I}_1 - 3)} - 1\right), \\
\mathcal{W}_{4,f}(\mathcal{I}_{4,\mathrm{f}}) &= \frac{a_\mathrm{f}}{2b_\mathrm{f}}\left(e^{b_\mathrm{f}\left((\mathcal{I}_{4,\mathrm{f}} - 1)_+\right)^2} - 1\right), \\
\mathcal{W}_{4,s}(\mathcal{I}_{4,\mathrm{s}}) &= \frac{a_\mathrm{s}}{2b_\mathrm{s}}\left(e^{b_\mathrm{s}\left((\mathcal{I}_{4,\mathrm{s}} - 1)_+\right)^2} - 1\right), \\
\mathcal{W}_{8,fs}(\mathcal{I}_{8,\mathrm{fs}}) &= \frac{a_\mathrm{fs}}{2b_\mathrm{fs}}\left(e^{b_\mathrm{fs}\mathcal{I}_{8,\mathrm{fs}}^2} - 1\right).
\end{aligned} \tag{11}$$

The symbol $(\cdot)_+$ indicates the positive part of the argument.

2.3 | Nearly-incompressible formulation

Although the constitutive law (10) is written for an incompressible material, in order to account for the effects of blood perfusion in the tissue we allow for small local volume changes adopting a nearly-incompressible formulation for the left ventricular muscle. For that we introduce a multiplicative decomposition of the deformation gradient tensor ([33])

$$\mathbf{F} = \bar{\mathbf{F}}\mathbf{F}_{\mathrm{vol}} \tag{12}$$

that is, the local deformation is the sequential application of a purely volumetric deformation $\mathbf{F}_{\mathrm{vol}}$, followed by an isochoric one $\bar{\mathbf{F}}$. For an isotropic material, the multiplicative decomposition (12) implies an additive decomposition of the strain energy into a volumetric and isochoric term. Anisotropic materials require more caution. In fact, by applying (12) to the constitutive law (10), the response of the tissue under a spherical state of stress would be isotropic. Following [34,35], we write (10) as

$$\mathcal{W}(\mathbf{C}) = \mathcal{W}_{\mathrm{iso}}(\bar{\mathcal{I}}_1) + \mathcal{W}_{\mathrm{a}}(\mathcal{I}_{4,\mathrm{f}}, \mathcal{I}_{4,\mathrm{s}}, \mathcal{I}_{8,\mathrm{fs}}) + \mathcal{W}_{\mathrm{vol}}(\mathcal{I}_3), \tag{13}$$

where $\bar{I}_1$ is the isotropic invariant of $\bar{\mathbf{C}} := \bar{\mathbf{F}}^T\bar{\mathbf{F}} = J^{-\frac{2}{3}}\mathbf{C}$. $\mathcal{W}_{\text{iso}}$ defines the isotropic material behavior under isochoric motion, while $\mathcal{W}_{\text{a}}$ contains the anisotropic response. The additional term $\mathcal{W}_{\text{vol}}$ is the energy term characterizing volume changes $J = \sqrt{I_3}$. It penalizes volume variations by making a deformation more energetically "expensive" when this is such that $J \neq 1$. Several expressions for $\mathcal{W}_{\text{vol}}$ are found in literature[36]: generally, an optimal choice is to consider a penalty function bounded (from below), convex and whose slope is null in $J = 1$. In this work, we use the following[37]:

$$\mathcal{W}_{\text{vol}}(J) = \frac{K}{4}(J^2 - 1 - 2\ln J). \tag{14}$$

Such volumetric energy is unbounded for $J \to 0$ or $J \to +\infty$ preventing the body to collapse into a point and to indefinitely dilate. The parameter K in (14) is called *bulk modulus*. The bulk modulus is a penalization factor that allows to weakly enforce incompressibility. The final form of the stress tensor reads as follows

$$\begin{aligned}\mathcal{P} = {} & ae^{b(\bar{I}_1-3)}J^{-\frac{2}{3}}\left(\mathbf{F} - \frac{1}{3}\mathbf{F}^{-T}\right) + \frac{K}{2}\left(J^2-1\right)\mathbf{F}^{-T} \\ & + 2a_{\text{f}}\left(\mathcal{I}_{4,\text{f}} - 1\right)_+ e^{b_{\text{f}}(\mathcal{I}_{4,\text{f}}-1)^2}\mathbf{f}\otimes\mathbf{f}_0 \\ & + 2a_{\text{s}}\left(\mathcal{I}_{4,\text{s}} - 1\right)_+ e^{b_{\text{s}}(\mathcal{I}_{4,\text{s}}-1)^2}\mathbf{s}\otimes\mathbf{s}_0 \\ & + a_{\text{fs}}\mathcal{I}_{8,\text{fs}}e^{b_{\text{fs}}\mathcal{I}_{8,\text{fs}}^2}\left(\mathbf{f}\otimes\mathbf{s}_o + \mathbf{s}\otimes\mathbf{f}_0\right).\end{aligned} \tag{15}$$

3 | ACTIVE CARDIAC MECHANICS: THE ACTIVE STRAIN APPROACH

Following the active strain model[18], we use a multiplicative decomposition of the deformation gradient tensor:

$$\mathbf{F} = \mathbf{F}_E\mathbf{F}_A,$$

into an elastic deformation $\mathbf{F}_E$ and an active deformation $\mathbf{F}_A$. The idea behind this formulation is that an inelastic process, driven by a microscopic force generation mechanism led by electrophysiology, locally and actively modifies the length and the shape of the fibers; then, an elastic deformation accommodates such active strain distortion in order to preserve the compatibility[18]. The physiological basis of this approach resides in the contractile units of the myocytes: $\mathbf{F}_A$ represents the sarcomeres shortening due to the sliding filaments of the actin–myosin molecular motor.

As explained in[18], the strain energy (13) only accounts for the elastic deformation; consequently, the Piola stress tensor is computed as

$$\mathbf{P}_E = \frac{\partial\mathcal{W}}{\partial\mathbf{C}_E}\frac{\partial\mathbf{C}_E}{\partial\mathbf{F}_E}. \tag{16}$$

By pulling back to the reference configuration by means of the Piola transformation of $\mathbf{F}_A$, we have

$$\mathbf{P} = \det(\mathbf{F}_A)\mathbf{P}_E\mathbf{F}_A^{-T}. \tag{17}$$

The expression of $\mathbf{F}_A$ must be provided according to a suitable constitutive law. Several descriptions of the active deformation $\mathbf{F}_A$ can be found in literature[19,25,20]. In particular, we compare the transmurally heterogeneous orthotropic activation model with the transversely isotropic and the orthotropic activation models.

3.1 | Transversely isotropic activation

Since fibers contract along their axis, to enable fiber shortening and preserve microscopic volume changes, a transversely isotropic activation model can be considered. In fact, myocytes do not significantly change their volume during contraction[38]. Therefore, a deformation along the fiber axis implies an isotropic deformation in the transverse plane to the fiber such that their volume is preserved. The active deformation gradient is assumed to take the form[24,25]

$$\mathbf{F}_A = \gamma_1\mathbf{f}_0\otimes\mathbf{f}_0 + \gamma_2(\mathbf{I} - \mathbf{f}_0\otimes\mathbf{f}_0), \tag{18}$$

where the contraction γ_1 occurs along fibers direction $\mathbf{f}_0$, while γ_2 accounts for the deformation in the transverse directions. We assume in the following that $\det(\mathbf{F}_A) = 1$, that is, the active deformations preserve volume of the myocyte. Specifically for the transversely isotropic activation model, this condition condition reads

$$\begin{aligned}1 = \det(\mathbf{F}_A) &= \frac{\left(\mathbf{F}_A\mathbf{f}_0\times\mathbf{F}_A\mathbf{s}_0\right)\cdot\mathbf{F}_A\mathbf{n}_0}{\left(\mathbf{f}_0\times\mathbf{s}_0\right)\cdot\mathbf{n}_0} \\ &= \frac{\left(\gamma_1\mathbf{f}_0\times\gamma_2\mathbf{s}_0\right)\cdot\gamma_2\mathbf{n}_0}{\mathbf{n}_0\cdot\mathbf{n}_0} = \gamma_1\gamma_2\mathbf{n}_0\cdot\gamma_2\mathbf{n}_0 = \gamma_1\gamma_2^2,\end{aligned} \tag{19}$$

so that we can write γ_2 in terms of γ_1 explicitly

$$\gamma_2 = \frac{1}{\sqrt{\gamma_1}}. \tag{20}$$

By taking $\gamma_1 = \gamma$ the final form of the active deformation gradient reads

$$\mathbf{F}_A = \gamma\mathbf{f}_0\otimes\mathbf{f}_0 + \frac{1}{\sqrt{\gamma}}(\mathbf{I} - \mathbf{f}_0\otimes\mathbf{f}_0). \tag{21}$$

3.2 | Orthotropic activation

In order to capture the physiological systolic wall thickening an alternative orthotropic model has been proposed in[20]. The authors use a multiscale argument to link the micro scale deformation occurring at the subcellular level with the macro scale deformation at the organ level. In particular, by assuming that the collagen fiber play an active role during contraction, by constraining the motion of the myocytes, the authors proposed an orthotropic activation model. In particular, the active deformation at micro scale is isochoric and it is described by means of the same transversely isotropic model described in Section 3.1. The active orthotropy originates from the inextensibility

of collagen fibers that wrap around the cardiac cells: contracting fibers enlarge in the directions orthogonal to their axis and this enlargement forces the fibers to rearrange inside the collagen sheet, thus increasing the myocardial wall thickness. With this model, the myocardium can easily thicken up to 40% during contraction[39], and such thickening is assumed to be carried out in virtue of mutual sliding of collagen sheets. Moreover, the orthotropic model introduces an additional parameter that one can exploit to better describe the muscle thickening occurring during contraction.

The micro scale active deformation is assumed to be in the form

$$\begin{aligned} \mathbf{F}_M &= \mathbf{I} + \xi_f \mathbf{f}_0 \otimes \mathbf{f}_0 + \xi_s \mathbf{s}_0 \otimes \mathbf{s}_0 + \xi_n \mathbf{n}_0 \otimes \mathbf{n}_0, \\ \det \mathbf{F}_M &= (1+\xi_f)(1+\xi_s)(1+\xi_n) = 1, \end{aligned} \tag{22}$$

where ξ_f, ξ_s and ξ_n are the microscopic deformations of fiber, sheet and normal respectively. The transverse isotropy requires that $\xi_s = \xi_n$ and the further assumption of isochoric deformation leads to $\xi_n = (1+\xi_f)^{-\frac{1}{2}} - 1$. By introducing an intermediate scale deformation where the cellular rearrangement takes place,

$$\mathbf{F}_S = \mathbf{I} + \zeta_s \mathbf{s}_0 \otimes \mathbf{s}_0 + \zeta_n \mathbf{n}_0 \otimes \mathbf{n}_0, \tag{23}$$

the macroscopic deformation tensor reads

$$\mathbf{F}_A = \mathbf{F}_S \mathbf{F}_M = \mathbf{I} + \gamma_{\mathrm{f}} \mathbf{f}_0 \otimes \mathbf{f}_0 + \gamma_{\mathrm{s}} \mathbf{s}_0 \otimes \mathbf{s}_0 + \gamma_{\mathrm{n}} \mathbf{n}_0 \otimes \mathbf{n}_0, \tag{24}$$

where $\gamma_j = \xi_j + \zeta_j + \zeta_j \xi_j$, for $j = f, s, n$ represent deformations at the macro-scale along fibers, sheets and cross-fiber directions. By using multiscale arguments, the authors in[20] relate the macroscopic deformations γ_{f}, γ_{s} and γ_{n} with the microscopic shortening of a single cell ξ_f such that

$$\gamma_{\mathrm{f}}\left(\xi_{\mathrm{f}}\right) = \xi_{\mathrm{f}}, \tag{25a}$$

$$\gamma_{\mathrm{n}}\left(\xi_{\mathrm{f}}\right) = k\xi_{\mathrm{f}}, \tag{25b}$$

$$\gamma_{\mathrm{s}}\left(\xi_{\mathrm{f}}\right) = \frac{1}{(1+\gamma_{\mathrm{f}})(1+\gamma_{\mathrm{n}})} - 1, \tag{25c}$$

where k is an orthotropic activation parameter which accounts for the collagen sheets rearrangement. The parameter k above can be used to fit experimental data. As in[20], we set the parameter $k = 4$. For more details on the derivation of the model, we refer the interested reader to the original paper[20].

3.3 | Transmurally heterogeneous orthotropic activation

Although the orthotropic model (Section 3.2) can easily capture the systolic wall thickening, the model fails to reproduce the heterogeneity of the deformation in the myocardium[20]. For this reason, starting from this orthotropic activation model, we develop a transmurally heterogeneous activation model. We assume that the sheet sliding is influenced by the tissue shearing induced by the torque exerted by the fibers. Due to the different orientations and lever arms of fibers at endocardium and epicardium, we assume that the larger lever arm at epicardium yields a larger deformation in the inner layers of the myocardium, thus causing a fibers rearrangement and resulting in increased wall thickness at endocardium. We model this myocardial behavior by considering a transmurally modulated orthotropic parameter $k(\lambda)$, where λ is the normalized transmural distance, such that $\lambda = 0$ at the endocardium while $\lambda = 1$ at the epicardium. The transmural distance λ is obtained using the Poisson interpolation, similarly to what presented in[40,20] to prescribe fibers field. This parameter is used to locally adapt the rearranging mechanism from endocardium, where the rearrangement occurs, to epicardium where the rearrangement is assumed to be negligible. In this way, we can extend the model (25) as follows

$$\gamma_{\mathrm{f}}\left(\xi_{\mathrm{f}}\right) = \xi_{\mathrm{f}}, \tag{26a}$$

$$\begin{aligned} \gamma_{\mathrm{n}}\left(\lambda, \xi_{\mathrm{f}}\right) &= k(1-\lambda)\xi_{\mathrm{f}} + \lambda\xi_{\mathrm{n}}, \\ &= k(1-\lambda)\xi_{\mathrm{f}} + \lambda\Big((1-\xi_f)^{-\frac{1}{2}} - 1\Big), \end{aligned} \tag{26b}$$

$$\gamma_{\mathrm{s}}\left(\lambda, \xi_{\mathrm{f}}\right) = \frac{1}{(1+\xi_{\mathrm{f}})(1+\gamma_{\mathrm{n}}\left(\lambda, \xi_{\mathrm{f}}\right))} - 1. \tag{26c}$$

Remark 1. At the endocardium ($\lambda = 0$), we have

$$\gamma_{\mathrm{f}}\left(\xi_{\mathrm{f}}\right) = \xi_{\mathrm{f}}, \tag{27a}$$

$$\gamma_{\mathrm{n}}\left(\lambda, \xi_{\mathrm{f}}\right) = k\xi_{\mathrm{f}}, \tag{27b}$$

$$\gamma_{\mathrm{s}}\left(\lambda, \xi_{\mathrm{f}}\right) = \frac{1}{(1+\xi_{\mathrm{f}})(1+k\xi_{\mathrm{f}})} - 1, \tag{27c}$$

coherently with (25).

4 | NUMERICAL APPROXIMATION

4.1 | Spatial discretization

The computational domain Ω_0 we use in our test is based on an idealized geometry for the ventricle described by half of a prolate ellipse[16]. The mesh is built from this geometry using linear tetrahedra and the meshing process has been carried out using Gmsh[41]. The meshing procedure introduces a partitioning $\mathcal{T}_h$ of the domain $\overline{\Omega}_0$ of non-overlapping elements such that $\Omega_{0,h} = \cup_{K \in \mathcal{T}_h} K$.

We choose the subspace V_h of V to be the finite element space of basis functions globally continuous and defined by Lagrange polynomials on each mesh element, i.e:

$$\begin{aligned} V_h = \Big\{ \mathbf{v}_h \in \left[C^0\left(\overline{\Omega}_{0,h}\right)\right]^3 : \left(\mathbf{v}_h\right)_i |_K \in \mathbb{P}_r \ \forall i = 1,2,3, \\ \forall K \in \mathcal{T}_h, \ \mathbf{v}_h \cdot \mathbf{N}_0 = 0 \ \text{on} \ \Gamma_{0,D} \Big\}. \end{aligned} \tag{28}$$

Since in this work we are interested in an accurate representation of the strains, which are related to the gradient of our solution, we use second order polynomials, that is $r = 2$. A generic function $\mathbf{v}_h$ of V_h can be expressed as a linear

combination of basis functions of (28)

$$\mathbf{v}_h(\boldsymbol{\xi}) = \sum_{i=1}^{M} v_i \boldsymbol{\phi}^i(\boldsymbol{\xi}), \tag{29}$$

where $\boldsymbol{\xi} \in \Omega_0$, M is the total number of degrees of freedom introduced by the spatial discretization and $\boldsymbol{\phi}^i$ is the ith Lagrangian basis function. In this context the displacement and the deformation gradient can be defined as

$$\mathbf{u}_h = \sum_{j=1}^{M} u_j \boldsymbol{\phi}^j(\boldsymbol{\xi}), \tag{30}$$

$$\mathbf{F}_h(\boldsymbol{\xi}) = \mathbf{I} + \sum_{j=1}^{M} u_j \nabla_0 \boldsymbol{\phi}^j(\boldsymbol{\xi}), \tag{31}$$

respectively. Then, we define $J_h = \det(\mathbf{F}_h)$ and $\mathbf{H}_h = J_h F_h^{-T}$. By introducing Gauss-Legendre quadrature rules over domain and boundaries, whose weights are $w(\boldsymbol{\xi}_q)$ and $w_{BD}(\boldsymbol{\xi}_q)$ respectively and by plugging (30) and (31) into (7), we derive the corresponding algebraic formulation for the elastostatic problem. By setting

$$L_i(\mathbf{u}_h) = \sum_{q=1}^{N_{Qpt}} w(\boldsymbol{\xi}_q) \left[\mathbf{P}\left(\mathbf{F}_h\left(\boldsymbol{\xi}_q\right)\right) : \nabla_0 \boldsymbol{\phi}^i(\boldsymbol{\xi}_q) \right], \tag{32}$$

$$B_i^N(\mathbf{u}_h) = \sum_{q=1}^{N_{BDQpt}} w_{BD}(\boldsymbol{\xi}_q) \left[p_v \mathbf{H}_h\left(\boldsymbol{\xi}_q\right) \mathbf{N}_0 \cdot \boldsymbol{\phi}^i(\boldsymbol{\xi}_q) \right], \tag{33}$$

$$B_i^R(\mathbf{u}_h) = \sum_{q=1}^{N_{BDQpt}} w_{BD}(\boldsymbol{\xi}_q) \left[\alpha \mathbf{u}_h \cdot \boldsymbol{\phi}^i(\boldsymbol{\xi}_q) \right], \tag{34}$$

the sum of (32), (33) and (34) yields the algebraic nonlinear system

$$\mathcal{L}(\mathbf{u}_h) = \mathbf{L}(\mathbf{u}_h) + \mathbf{B}^N(\mathbf{u}_h) + \mathbf{B}^R(\mathbf{u}_h) = \mathbf{0}. \tag{35}$$

4.2 | Solution of the nonlinear problem

We solve the nonlinear problem (35) by the Newton-Raphson method[42,43]. The method exploits information from the Jacobian $\boldsymbol{J}$ of $\mathcal{L}(\mathbf{u})$ to achieve the solution of the nonlinear problem:

$$\begin{aligned}
J_{ij}(\mathbf{u}_h)\delta u_j &= \lim_{\varepsilon \to 0} \frac{\mathcal{L}_i(\mathbf{u}_h + \varepsilon \delta \mathbf{u}_j) - \mathcal{L}_i(\mathbf{u}_h)}{\varepsilon} \\
&= \sum_{q=1}^{N_{Qpt}} w_q \nabla_0 \boldsymbol{\phi}_q^i : \frac{\partial \mathbf{P}}{\partial \mathbf{F}}\left(\mathbf{F}_h\left(\boldsymbol{\xi}_q\right)\right) \left[\delta u_j \nabla_0 \boldsymbol{\phi}_q^j \right] \\
&+ \sum_{q=1}^{N_{BDQpt}} w_{BD,q} \boldsymbol{\phi}_q^i \cdot \Bigg[\alpha \delta u_j \boldsymbol{\phi}_q^j \\
&+ \quad p_v \Big[\left(\mathbf{F}_h^{-T}\left(\boldsymbol{\xi}_q\right) : \delta u_j \nabla_0 \boldsymbol{\phi}_q^j \right) \mathbf{I} \\
&- \mathbf{F}_h^{-T}\left(\boldsymbol{\xi}_q\right) \left(\delta u_j \nabla_0 \boldsymbol{\phi}_q^j \right)^T \Big] \mathbf{H}_h\left(\boldsymbol{\xi}_q\right) \mathbf{N}_0 \Bigg],
\end{aligned} \tag{36}$$

where we denote with $\delta \mathbf{u}_j = \delta u_k \delta_{k,j}$, $w_q = w(\boldsymbol{\xi}_q)$, $w_{BD,q} = w_{BD}(\boldsymbol{\xi}_q)$ and $\boldsymbol{\phi}_q^j = \boldsymbol{\phi}^j(\boldsymbol{\xi}_q)$. The fourth order tensor $\partial \mathbf{P}/\partial \mathbf{F}$ depends only on the constitutive assumptions of the material and it is computed from the strain energy density function as

$$\frac{\partial \mathbf{P}}{\partial \mathbf{F}} = \frac{\partial^2 \mathcal{W}}{\partial \mathbf{F} \partial \mathbf{F}}. \tag{37}$$

Given an initial guess $\mathbf{u}_h^0$, the solution of (35) is achieved as the limit (should it exist) of the sequence $\{\mathbf{u}_h^n\}$, such that

$$\mathbf{J}(\mathbf{u}_h^n)\delta \mathbf{u}^{n+1} = -\mathcal{L}(\mathbf{u}_h^n) \tag{38}$$

$$\mathbf{u}_h^{n+1} = \mathbf{u}_h^n - \delta \mathbf{u}^{n+1}. \tag{39}$$

The stopping tolerance of the Newton method is set 10^{-7} over the ∞-norm of the residual $\mathcal{L}(\mathbf{u}_h^n)$.

Remark 2. Taking advantage of the flat surface at left ventricle base as seen in Fig. 1 a, with normal vectors aligned along one of the cartesian axes, the Dirichlet boundary condition is enforced algebraically by manipulating the rows of the matrix:

$$J_{j_D j} = \delta_{j_D, j} \quad \text{for } j = 1, .., M, \tag{40}$$

$$\mathcal{L}_{j_D} = \delta \bar{u}_{j_D}^n \delta_{n,0}, \tag{41}$$

being j_D the index identifying a Dirichlet node and $\delta \bar{u}_{j_D}$ the value of the boundary condition.

Remark 3. The non-symmetric linear system (36) is resolved using GMRES with an algebraic additive Schwarz preconditioner with local exact LU decompositions[44].

5 | NUMERICAL RESULTS

We use a prolate ellipsoidal geometry fitted from the one used in[16] by setting the same focal length of 2.91 cm, cavity volume of 37 mL and a wall volume of 125 mL. The geometry is described by the prolate ellipsoidal coordinates

$$x = d \sinh(\xi) \sin(\theta) \cos(\phi), \tag{42}$$

$$y = d \sinh(\xi) \sin(\theta) \sin(\phi), \tag{43}$$

$$z = d \cosh(\xi) \cos(\theta), \tag{44}$$

where d is the focal length, $\xi \in [0.6, 1.02]$, $\phi \in [0, 2\pi]$ and $\theta \in [\theta_0(\xi), \pi]$, with $\theta_0(\xi)$ such that the base is located at $z = 1.19$ cm. Three meshes have been generated using mesh size of 1.0 cm, 0.7 cm and 0.5 cm, respectively. An example is shown in Fig. 2 . Since we compare strains resulting from our simulation with those reported in[16], we need to modify the constitutive parameters of our model in order to match those in[16]. To adapt our active strain implementation of the Holzapfel-Ogden constitutive law, we applied a least-square fitting strategy to match parameters from Guccione law[16] using an approach similar to[45]. The result of the fitting is presented in Table 1 .

The fiber and cross-fibers directions $\mathbf{f}_0$ and $\mathbf{n}_0$ are taken in an orthonormal system. We assume the collagen sheets to have a radial distribution. The fiber direction changes transmurally

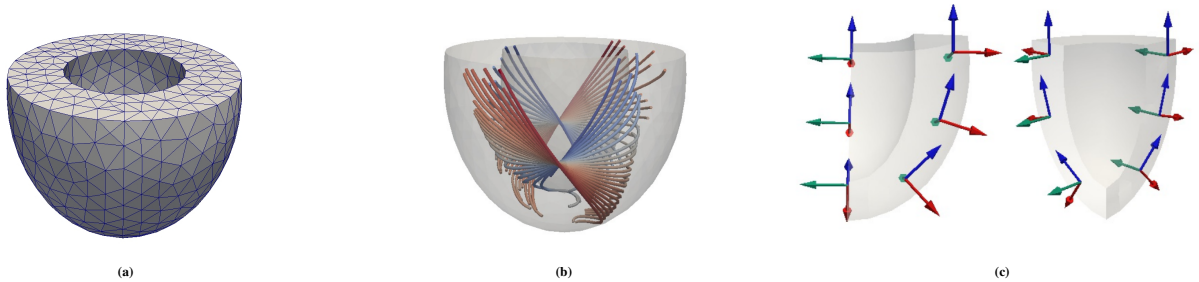

FIGURE 2 View of the mesh used for the strains analysis (a); the mesh comprises 668 vertices and 2380 tetrahedra. Transmurally symmetric distribution of the fibers (b); these are oriented with an helix angle ranging from -60° at epicardium to +60° to endocardium. Orthogonal triplets corresponding to the longitudinal (blue), radial (red), circumferential (green) directions (c); (c) shows also collagen sheets orientation since these are oriented along the radial direction.

and linearly from −60° at epicardium to +60° at endocardium, while the cross-fiber direction goes from +30° at epicardium to −30° at endocardium. In our analysis we consider the distribution of strains and shear strains both in space and time. In particular, by denoting with **c**, **l**, **r** the circumferential, the longitudinal and the radial directions respectively, as shown in Fig. 2 c, we define the following strains

$$E_{cc} = \mathbf{Ec}\cdot\mathbf{c}, \qquad E_{ll} = \mathbf{El}\cdot\mathbf{l}, \qquad E_{rr} = \mathbf{Er}\cdot\mathbf{r},$$
$$E_{cl} = \mathbf{Ec}\cdot\mathbf{l}, \qquad E_{cr} = \mathbf{Ec}\cdot\mathbf{r}, \qquad E_{lr} = \mathbf{El}\cdot\mathbf{r},$$

where $\mathbf{E} = \frac{1}{2}(\mathbf{C}-\mathbf{I})$ is the Green–Lagrange finite strain tensor. The above strains will be evaluated to compare our results with those in literature.

5.1 | Convergence test under h-refinement

We solve the problem with three isotropic meshes with mesh size h=1.0, 0.7, and 0.5 cm. We set the boundary conditions as in (5), with $\alpha = 3.75$ mmHg/cm in (5e). We model the activation with the transmurally varying orthotropic model, with k=4. Each simulation consists of an entire cardiac cycle, which is divided in two main phases: diastole and systole. Each phase can be further split into a stage of null intraventricular flow rate (isochoric relaxation for diastole and isochoric contraction for systole) and a stage characterized by blood circulation (filling during diastole and ejection during systole). In this context, "isochoric" means that the deformation preserves the intraventricular volume. The four phases are governed by a relation between the cavity volume and the cavity pressure that can be represented in a pressure-volume loop diagram. In this test, the cycle starts with a preload ramp which inflates the ventricular cavity. This is achieved by setting increasing uniform pressure values on the endocardial surface until reaching the value p_{mvc}, the pressure at which the mitral valve closes. A system of idealized 0D valves is used to control the circulation of blood and prevents reverse flow due to pressure differences. The mitral valve allows flow entering the left ventricle whenever the ventricular preload (p_{mvc}) is larger than the cavity pressure. Once the preload pressure is reached, the idealized mitral valve closes. At this stage, we initiate fibers activation by setting a uniform value for γ_{f} throughout the computational domain. The fibers start to contract determining the onset of the isochoric systolic phase. The evolution in time of the active strain is prescribed using the relation

$$\gamma_{\mathrm{f}}(t) = \gamma_{\mathrm{f,min}} \sin^2\left(\pi \frac{t-t_0}{t_F - t_0}\right), \tag{45}$$

where t_0 and t_F are the initial and final times of the simulation and $\gamma_{f,min}$ is the minimum value of the active strain (the largest in modulus). In this test, we set $\gamma_{\mathrm{f,min}} = -0.13$. The evolution of the active strain γ_{f} is shown in Fig. 3 b.

During the isochoric phase, the ventricular pressure is unknown. Therefore, we look for a pressure value that keeps the cavity volume constant. With this aim, we use the fixed point iterative algorithm:

$$\begin{cases} C_v^n = V_v^n / p_v^n, \\ p_v^{n+1} = p_v^n + \dfrac{\Delta V_v^n}{C_v^n}, \end{cases} \tag{46}$$

where n is the iteration number, p_v^n is the cavity pressure and $\Delta V^n = V^n - \bar{V}$ is the variation of the cavity volume. $\bar{V}$ is equal to the end diastolic cavity volume during isochoric contraction and equal to end ejection cavity volume during isochoric relaxation. When the cavity pressure reaches the aortic pressure (initialized at p_{AVO}) at time t_{BE}, we set a dynamic afterload by coupling the cavity pressure with a two-element Windkessel model[46].

$$C_{wk}\frac{dp_v}{dt} = Q_v - p_v/R_{wk}, \quad t \in [t_{BE}, t_{EE}], \tag{47}$$

where t_{BE}, t_{EE} are time of begin ejection and time of end ejection respectively, p_v equals the aortic pressure as long as the aortic valve is open, $p_v(t_{BE})$ is the pressure value at which the

a [kPa]	b	a_f [kPa]	b_f	a_s [kPa]	b_s	a_{fs} [kPa]	b_{fs}
0.20000	4.6140	4.1907	7.8565	2.5640	10.446	0.13040	15.255

TABLE 1 Parameters obtained from the least-square fitting of the Cauchy stress tensor.

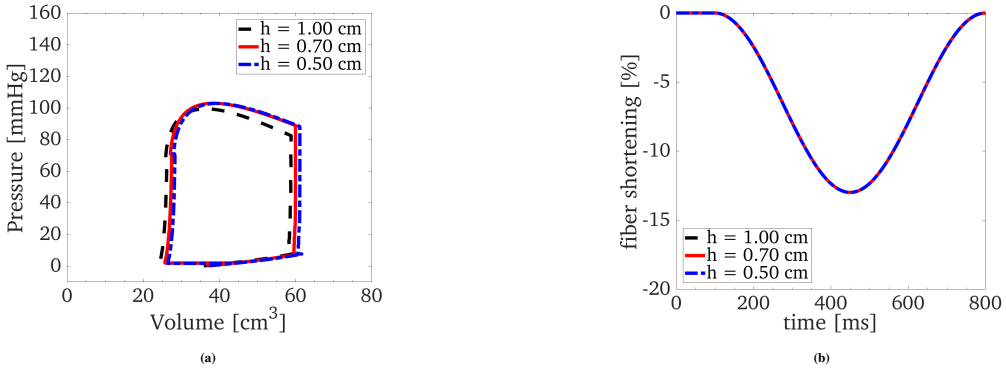

FIGURE 3 Simulations of a cardiac cycle using different mesh sizes h=1.00, 0.75 and 0.50 cm. In (a) we represent the pressure-volume diagrams obtained with the three meshes. In (b) we depict the evolution of the active strain activation γ_f vs. time.

valve opens and Q_v is the outward flow rate from the ventricle. This phase continues until a positive value of Q_v persists. As fibers start to relax, the flow rate becomes negative and the aortic valve closes, preventing the reversed flow and initiating the diastolic isochoric phase. Once again the same isochoric process described before occurs, which is caused by the cavity pressure dropping below aortic one. The cavity volume does not change until a final pressure (p_{mvo}) is achieved and the mitral valve opens, thus letting the blood to fill again the chamber. The simulation ends when fibers stop relaxing. The overall process can be observed in Fig. 6 b. Values used for this simulation are shown in Tab. 2 . The overall procedure is summarized in Algorithm 1.

The results of the mesh convergence test under h-refinement are shown in Fig. 3 and in Fig. 4 . Fig. 3 a shows the pressure–volume diagrams. We obtained three pressure–volume loops which mainly differ for the end diastolic volume. From the coarsest mesh (black dashed line) to the finest one (dotted blue line) the maximum difference in terms of strain throughout the cardiac cycle decreases and we obtain that part of the intermediate mesh loop (solid red line) is superimposed on the blue line. Fig. 4 a-Fig. 4 f report the relation between strains and shear strains, averaged in the equatorial area of the ventricle, and the activation parameters γ_f (in modulus), representing the active fiber shortening. This representation helps the interpretation of the results for its similarity with the pressure–volume diagram in Fig. 3 a since the positive correlation between $|\gamma_f|$ and the cavity pressure and the correlation between cavity volume and strains. The cardiac cycle starts with $\gamma_f = 0$, then a horizontal segment determines the sign of the correlation between strains and $|\gamma_f|$: positive for anti-clockwise loops Fig. 4 a-4 b-4 d-4 f and negative for clockwise loops Fig. 4 c and 4 e, as indicated by the red arrow. The strains, except for Fig. 4 d, present a four angles shape. Each angle represent a change in the cardiac phase. Starting from zero, the unloaded configuration, the initial horizontal segment corresponds to the passive inflation. Then, the ascending curve represents the systolic phase made of isovolumic contraction and ejection, the descending part shows the diastolic phase made of isovolumic relaxation and filling. From Figs. 4 a-4 c we see that the loops related to axial strains vary the most with the choice of the mesh. We deduce that the axial strains are more significantly affected by the discretization error than shear strains, in particular the circumferential strain which varies of the 25% from the coarse to the finest mesh at both end diastolic and end systolic stages. The ventricle's average radius and length increase when inflated and the wall thickness decreases (as deduced from Fig. 4 a, Fig. 4 b and Fig. 4 c). These quantities remain approximately constant during both isovolumic phases. During the ejection phase the ventricular radius and its length both decrease, while the wall thickness increases to preserve the wall volume. Finally, during the relaxation phase, the ventricle returns to the initial unloaded configuration. The shear strains are depicted in Figs. 4 d-4 f. Fig. 4 d shows the circumferential-longitudinal shear strain, the one related with ventricular torsion. E_{cl} describes the longitudinal gradient of planar rotation. With

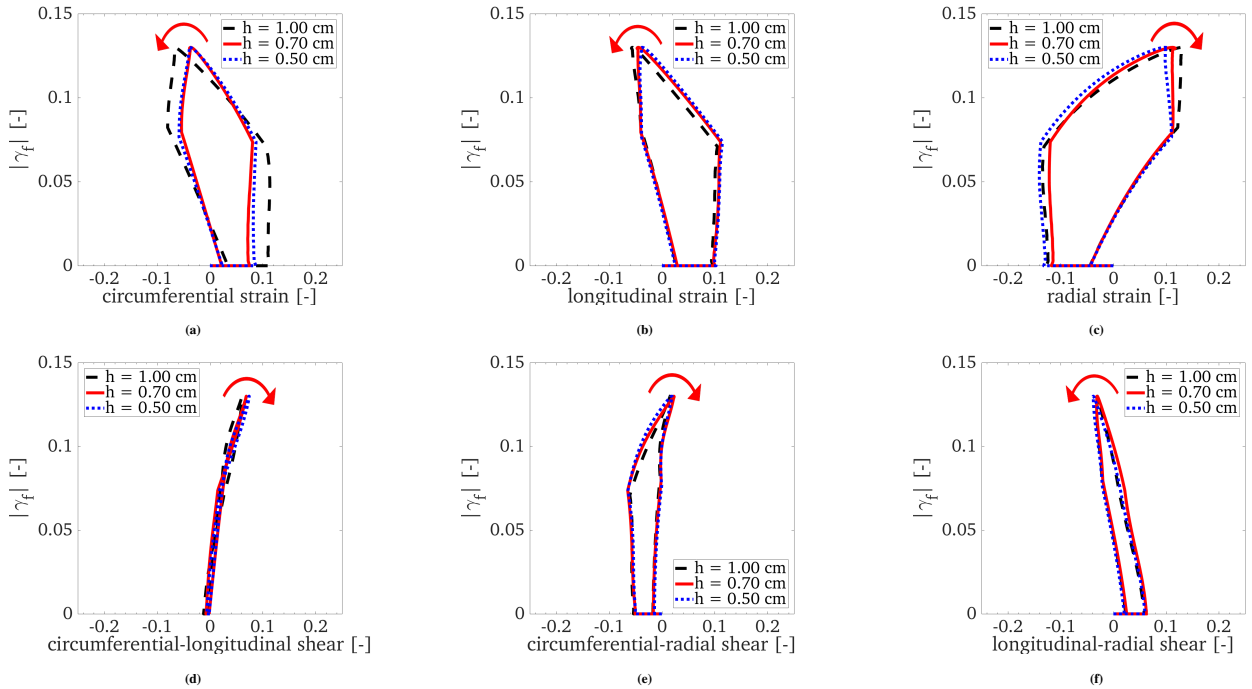

FIGURE 4 Simulations of a cardiac cycle using different mesh sizes h=1.00, 0.75 and 0.50 cm. γ_f vs. average equatorial strains (top) and shear strains (bottom).

p_{mvc}	p_{avo}	p_{mvo}	R_{wk}	C_{wk}
1 kPa	10 kPa	0.25 kPa	80000 kPa ms/ml	0.00165 ml/kPa

TABLE 2 Parameters used in simulations to regulate the cardiac cycle.

respect of the coordinate system shown in (Fig. 2 c), a positive circumferential-longitudinal shear strain E_{cl} means that the rotation of the upper side of the ventricle is larger than the lower part, where positive rotation are counter-clockwise with respect of the apex to base axis. The circumferential-radial shear strain E_{cr} describes the radial gradient of planar rotation. Fig. 4 e shows that this rotation gradient is always negative apart from a short lapse of time between the final stage of ejection and isochoric relaxation when it becomes positive. The interpretation is the following: when E_{cr} is positive means that the rotation angle at epicardium is larger than the one at endocardium; when it is negative, the rotation angle is larger at endocardium. This can be appreciated also in Fig. 5 e, where the endocardium rotates clockwise along the apex-to-base axis while the epicardium rotates counter-clockwise. Conversely, the longitudinal-radial shear strain E_{lr} is positive for almost the whole cardiac cycle apart between the last stage of the ejection and the initial stage of isovolumic relaxation when it becomes slightly negative. The interpretation of this shear is less straightforward. A positive value of this shear means that the angle between the deformed longitudinal direction and the deformed radial direction is an acute angle, thus inducing a tapered shape to the ventricle. A negative value of this shear strain means that the ventricle tends to assume a spherical shape.

From the plots in Fig. 4 , we observe that the axial strains are those more affected by the choice of the mesh. However, the intermediate mesh, with h =0.7 cm, yields accurate results and limits the computational cost. Therefore, hereafter, we use the mesh with mesh size h=0.7 cm as it already provides an accurate description of the strains.

5.2 | Calibration of epicardial Robin coefficient α during passive inflation

As stated in Section 2, we set Robin boundary conditions at the epicardium (see (5e)). The parameter α in the Robin condition is not know a priori. In order to choose it, we perform a passive inflation test of the left ventricle and we compare the strains obtained numerically against the experimental measurements in[47]. We finally select the value of α that better matches the experiments.

We perform several numerical simulations using the same preload pressure p_{mvc} of 1 kPa for different values of the Robin coefficient α ranging from 75 mmHg/cm (stiffer) to 0.75 mmHg/cm (softer). In Fig. 5 we show the three axial strains and the three shear strains: circumferential (E_{cc}), longitudinal (E_{ll}), radial (E_{rr}), circumferential-longitudinal (E_{cl}), circumferential-radial (E_{cr}) and longitudinal-radial (E_{lr}). We also show the experimental strain measurements from[47] depicted with bars indicating their standard deviation. The computationally evaluated strain are taken at equatorial height of the ventricle in agreement with the reference data.

As it can be seen in Figs. 5 a, 5 b, 5 c, the axial strains are in very good qualitative and quantitative agreement with the measurements when a small value of α is set. In particular, circumferential and radial strains converge within the experimental range by lowering the stiffness of the surrounding material, thus indicating that the myocardium itself is able to absorb the elastic energy by counter-balancing the cavity pressure with its stiffness. Conversely, the longitudinal strain (E_{ll}), which during diastole describes the elongation of the ventricle, does not match within experimental range by lowering α. By considering that both E_{ll} and the intraventricular volume agree with experimental data, a possible explanation of this outcome is that the elastic energy related to longitudinal strains is not completely absorbed by the myocardium but is partially absorbed by the deformation of the surrounding tissue. In particular, the pericardium has an important role in this mechanism as experimentally noted also in[48], where the authors evidenced how the pericardium enforces the stiffness of the myocardium during diastole.

Regarding shear strains, a qualitative agreement is obtained for circumferential-longitudinal (E_{cl}) shear for every value α considered. For circumferential-radial (E_{cr}) and longitudinal-radial (E_{lr}) shears the match is unsatisfactory for every choice of the parameter α. Shear strains do not appear to be affected by Robin boundary condition at epicardium, but rather by constitutive assumptions. For this reason, in this test we do not take these data into account to calibrate the Robin coefficient. Following this analysis, we set $\alpha = 7.5$ mmHg/cm in numerical simulations considering the qualitatively good agreement with experimental data in terms of axial strains and the physiological filling volume obtained in agreement with[47].

5.3 | Comparison of active contraction models

We compare the cardiac cycles for the three activation models described in Sec. 3. The cardiac cycle simulation has been discussed in Sec. 5.1 and it is summarized in Algorithm 1. Additionally, the Robin coefficient in Eq. (5) is set to $\alpha = 7.5$

Algorithm 1 Algorithm sketching the different phases within the cardiac cycle. The input data for a simulation consist in the pacing time of the ventricle (t_{ed}), the activation profile in time ($\gamma_f(t)$), the constitutive parameters of the circulation model (C_{wk} and R_{wk}, compliance of the artery and resistance of the peripheral circulation) and the pressures at which valves operate (p_{mvc}, mitral valve closing pressure, p_{avo} aortic valve opening pressure and p_{mvo} mitral valve opening pressure). The algorithm starts with a ramp that brings the ventricular pressure to p_{mvo}, then fibers shortening takes place and the mechanics is iteratively solved to preserve cavity volume V_{ed} (46). When cavity pressure, p_v, exceeds p_{avo}, subsequent resolutions of the mechanics and the circulation model occurs to couple the blood flows, following (47). Just as the outgoing flow Q_v vanishes, the end systolic cavity volume is preserved by solving the mechanics using (46) once again, this time while fibers are relaxing. When p_v drops below p_{mvo} the pressure is kept equal to the preload pressure and the ventricle fill up again due to fibers relaxation.

Require: $t_{ed}, \gamma_f(t), C_{wk}, R_{wk}, p_{mvc}, p_{avo}, p_{mvo}$
if $0 \le t \le t_{ed}$ **then** ▷ Filling
  $p(t) = (t/t_{ed})\, p_{mvc}$
  $\delta x, V_{ed} \leftarrow$ solve mechanics
else
  if $p(t) \le p_{avo}$ **then** ▷ Isochoric Contraction
    $\gamma_f = \gamma_f(t)$
    while $|\delta V| > tol$ **do**
      $p_v^k(t) = p_v^{k-1}(t) - \frac{V_v^{k-1} - V_{ed}}{C_v^{k-1}}$
      $\delta x_k, V_v^k, C_v^k \leftarrow$ solve mechanics
    end while
  else ▷ Ejection
    $\gamma_f = \gamma_f(t)$
    while $Q_v(t) > 0 \quad \& \quad |Q_v - Q_c - Q_r| > tol$ **do**
      $p_v^k(t) = \frac{(Q_v^{k-1}(t) + C_{wk}\frac{p_v^{k-1}}{dt})}{(\frac{C_{wk}}{dt} + \frac{1}{R_{wk}})}$
      $\delta x_k, Q_v^k = -\frac{dV_v^k}{dt} \leftarrow$ solve mechanics
    end while
    $V_{ee} = V_k$
    if $p_v(t) > p_{mvo}$ **then** ▷ Isochoric Relaxation
      $\gamma_f = \gamma_f(t)$
      while $|\delta V| > tol$ **do**
        $p_v^k(t) = p_v^{k-1}(t) + \frac{V_v^{k-1} - V_{ee}}{C_v^{k-1}}$
        $\delta x_k, V_v^k, C_v^k \leftarrow$ solve mechanics
      end while
      $\bar{p}_v = p_v^k(t)$
    else ▷ Relaxation
      while $\gamma_f < 0$ **do**
        $\gamma_f = \gamma_f(t)$
        $p_v(t) = \bar{p}_v$
        $\delta x(t) \leftarrow$ solve mechanics
      end while
    end if
  end if
end if

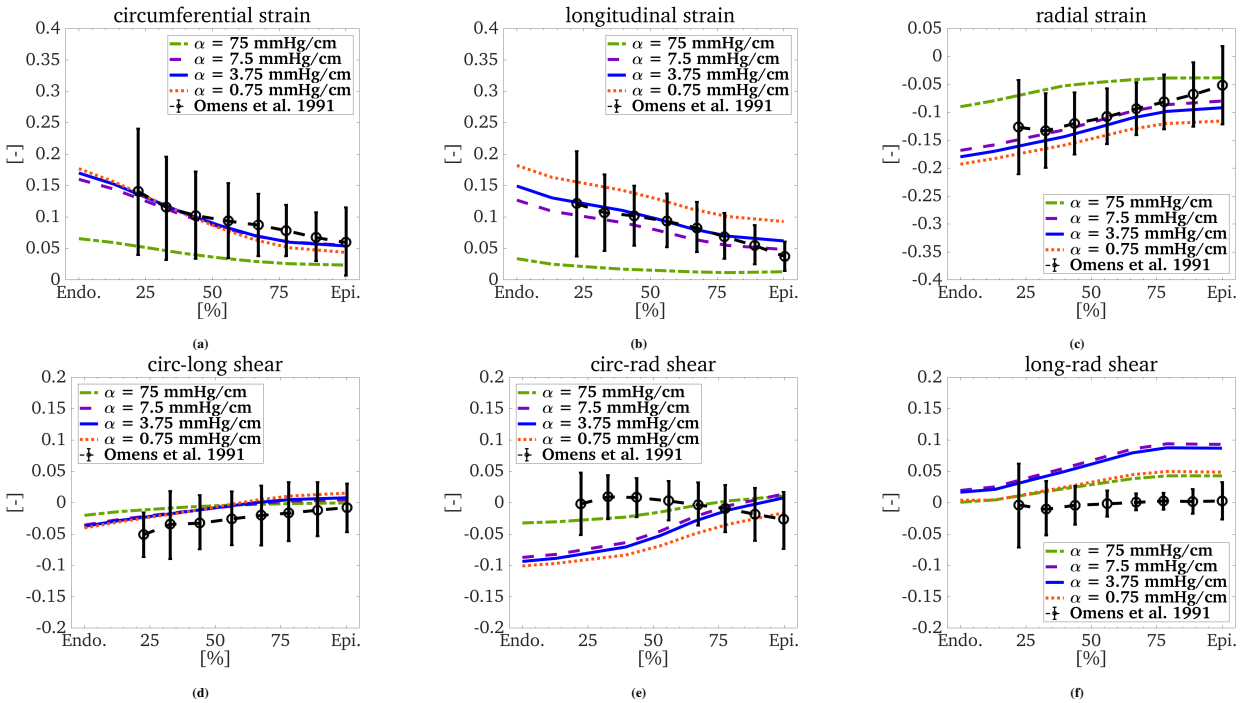

FIGURE 5 Comparison of the end-diastolic strains using different Robin coefficients for the epicardial boundary condition. Top row: axial strains (from left to right E_{cc}, E_{ll} and E_{rr}). Bottom row: shear strains (from left to right E_{cl}, E_{cr} and E_{lr}). Strains, both experimental and numerical, are measured through the myocardium at equatorial height. Strains are represented over wall thickness expressed in percentage. Experimental data are reported with error bars indicating standard deviations. The endocardial pressure was set to 1 kPa (7.5 mmHg) according to experiment in[47].

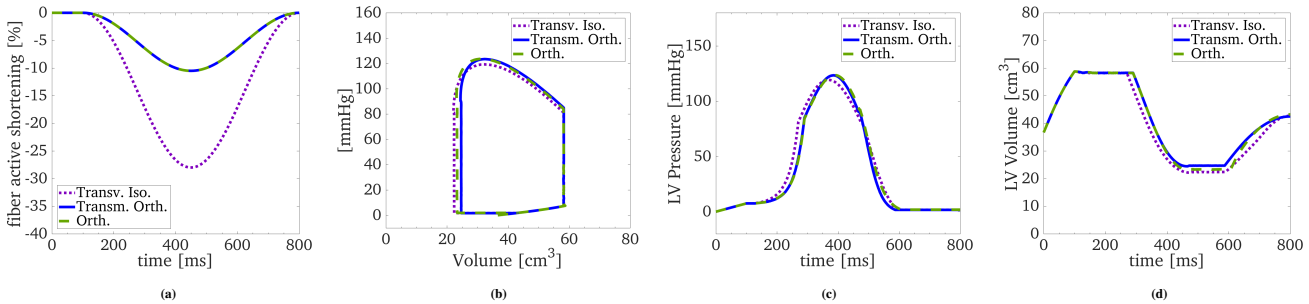

FIGURE 6 (a) Time evolution of the active strain γ_f; (b) pressure-volume diagrams; (c) left ventricular cavity pressure and 6 d) left ventricular cavity volume throughout the cardiac cycle.

mmHg/cm. This choice, which we discussed in Sec. 5.2, allows us to better match the diastolic strains.

The evolution of the activation γ_f is prescribed using Eq. (45). The maximum active shortening ($\gamma_{f,min}$) is tuned in each model in order to obtain a similar ventricular ejection fraction. In this way, we compare the models under similar hemodynamics conditions. The γ_f function is reported in Fig. 6 a for the three activation models. Here we observe that, while for models that incorporate multiscale effects the maximum active shortening lays inside a physiological range between -0.1 and -0.15, for the transversely isotropic activated material γ_f lays outside this range. In particular, we set $\gamma_{f,min} = -0.28$ for the transversely isotropic activation model and $\gamma_{f,min} = -0.105$ for the orthotropic model and for the heterogenous orthotropic model, using an orthotropic activation parameter $k = 4$ and $k = 5.5$ respectively.

Fig. 6 b shows a comparison of the pressure-volume loops obtained with the three activation models under consideration. The three curves are close enough to enable comparisons of the strains at final systolic stage. Figs. 6 c and 6 d suggest that

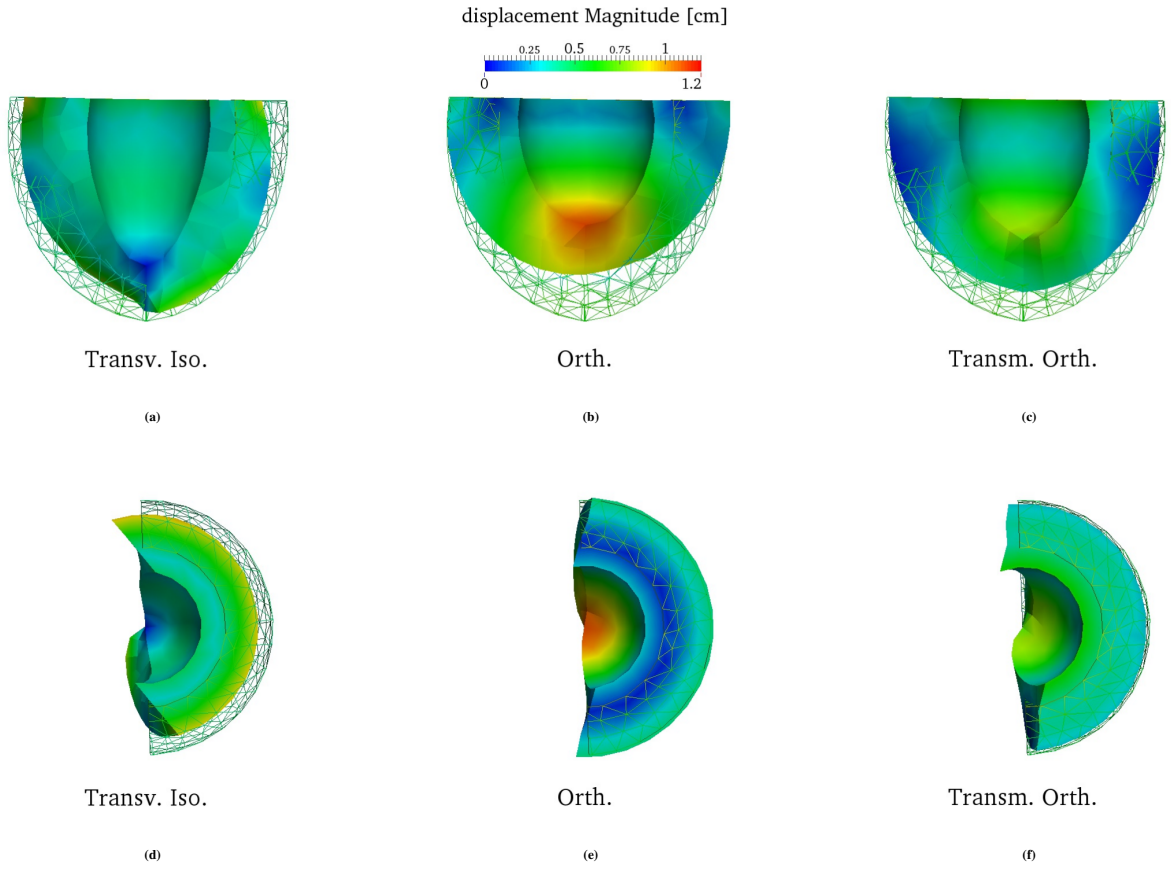

FIGURE 7 3D deformation of the three activation models at p_v=14 kPa over the end diastolic configuration.

the transversely isotropic model has a slightly different pressure development, most probably due to the larger increments in the fibers shortening which determine a different timing in the opening/closing of valves. Despite this small delay, the pressure-volume loop in Fig. 6 b shows that the end-systolic comparison at 14 kPa can be made at almost same ejection fraction (about 60%).

Fig. 7 shows the deformed configuration in which we computed strains (shown in Fig. 8) at $p_v = 14$ kPa of cavity pressure. The top row shows the side view of a section of the idealized ventricle. The bottom row shows the deformed cavities and the basal planes. We show the transversely isotropic model, the orthotropic model and the transmurally heterogeneous orthotropic model from left to right. The side view highlights the different behaviors of the two orthotropic models: they both exhibit a similar shortening and wall thickening, while the transversely isotropic model has a smaller ventricular shortening and a more elongated shape. The basal view highlights that the three models have different behaviors in terms of rotation (in-plane rotation) and torsion (rotation gradient: offset between basal and apical rotations). The transversely isotropic model and the transmurally heterogeneous orthotropic models have coherent torsion but an opposite in-plane rotation, suggesting that the two models should have similar values for the circumferential-longitudinal shear strains E_{cl} but different circumferential-radial shear strain E_{cr} (see Figs. 8 d and 8 e). The orthotropic model exhibit both rotation and torsion reversed with respect to the transversely isotropic model. The comparison of shear strains with experimental data confirms that the correct behavior is the one presented by the transmurally orthotropic activation model (Fig. 7 f).

Starting from circumferential strains in Fig. 8 a, the two orthotropic models yield results close to the experimental data while the transversely isotropic activation has larger circumferential shortenings. As depicted in Fig. 7 a, this results in an excessive reduction of the cross-sectional area of the ventricular cavity. According to experimental data, this behavior seems to be unphysiological. By observing Fig. 8 b, the transversely isotropic activation provides longitudinal strains in qualitative agreement with the experiments for the longitudinal strains. As shown in Fig. 7 b, the shortening occurring in the orthotropic activation model, is too large and resides outside experimental data range. The transmurally heterogeneous orthotropic activation model provide longitudinal strain slightly outside the

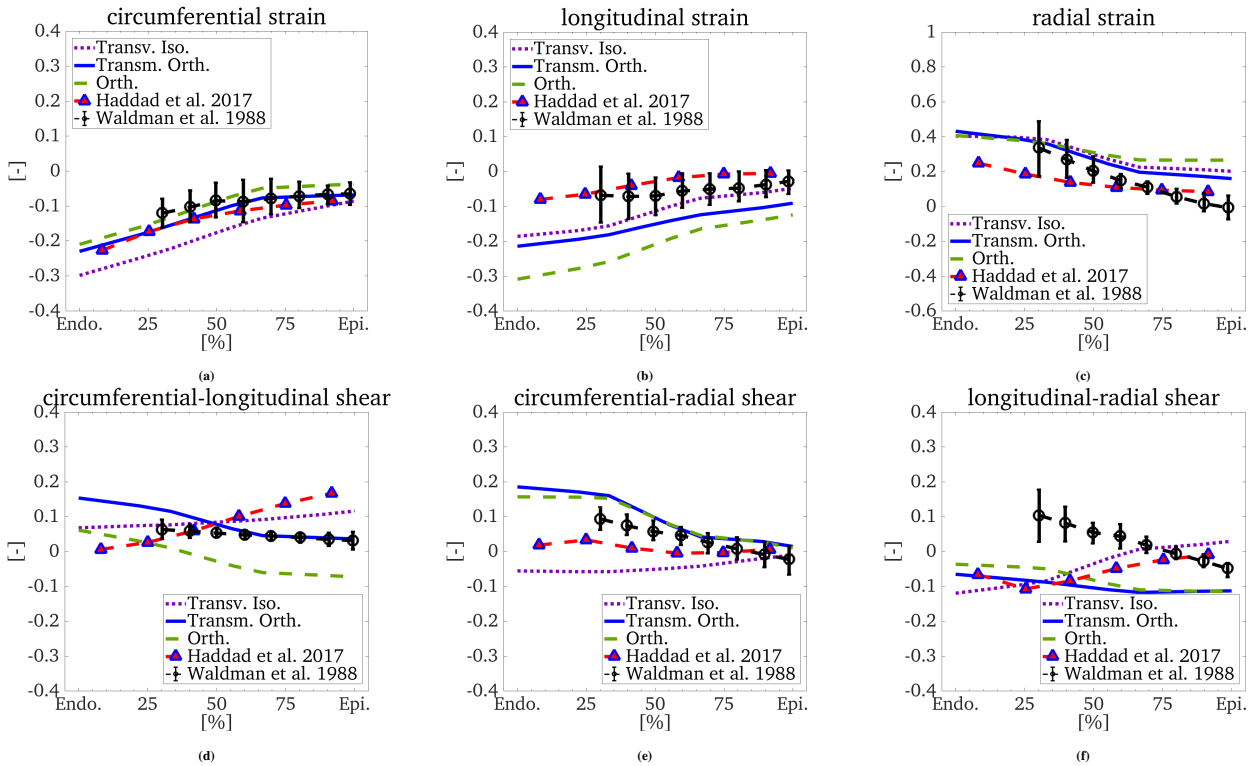

FIGURE 8 Comparison of the systolic strains at cavity pressure $p_v = 14$ kPa. The strains are evaluated at equatorial height and plotted vs. the normalized transmural length. The three lines with no markers represent results stemming the transversely isotropic (··), orthotropic (–), and transmurally heterogeneous orthotropic (-) active strain model. The marked line shows results using the active stress model of[17], the error bars, instead, experimental measurements from[47].

experimental data range and qualitatively close to the predicted by the transversely isotropic activation model. Considering radial strains E_{rr}, the three models well describe wall thickening at endocardium. However, all of them fall off from the experimental range at epicardium, even though the transmurally orthotropic activation model presents a slightly improved prediction. By checking the circumferential-longitudinal shear strain E_{cl} against the experimental data in Fig. 8 d, we deduce which activation model is capable of correctly reproducing the ventricular torsion. The orthotropic models fail to properly represent torsion since provides torsion in the opposite direction. The transversely isotropic activation model instead, despite predicts torsion close to the experimental range, it shows a reversed transmural distribution (strains increasing from endocardium to epicardium, instead of decreasing). This is also confirmed by the circumferential-radial shear strains – related closely to in-plane rotation – shown in Fig. 8 e, where the transversely isotropic model has opposite sign with respect to the experimental data. The transmurally heterogeneous orthotropic model proposed in this paper captures the ventricular torsion correctly. Finally, Fig. 8 f shows that none of the models herein analyzed is able to provide a good qualitative match of the longitudinal radial shear strains E_{lr}. One possible reason for this behavior is that longitudinal-radial shear strains E_{lr} are affected by the orientation of the fiber field, which we maintained fixed for all the simulations.

Additionally, we compare our results with those obtained for the left ventricular systolic strain using instead an active stress formulation[17]. We represent the strains computed with the active stress model with a dashed blue line and a triangular marker in Fig. 8 . The active stress formulation has a similar behavior in terms of circumferential strains where both orthotropic models fit the experimental data within one standard deviation. In the longitudinal and radial directions, the strains are more accurate using the active stress formulation of[17]. However, the active stress formulation is unable of reproducing any of the shear strains. In particular, similarly to what obtained using the transversely isotropic active strain model, the circumferential-longitudinal strains E_{cl} increase from endocardium to the epicardium. This behavior is opposite to the one shown in the experimental data. The circumferential-radial shear strains are better captured but qualitatively far from the experimental data. However, a small planar rotation is evident in the correct direction. As for the active strain model, also the active stress formulation is unable to predict the longitudinal-radial shear strains.

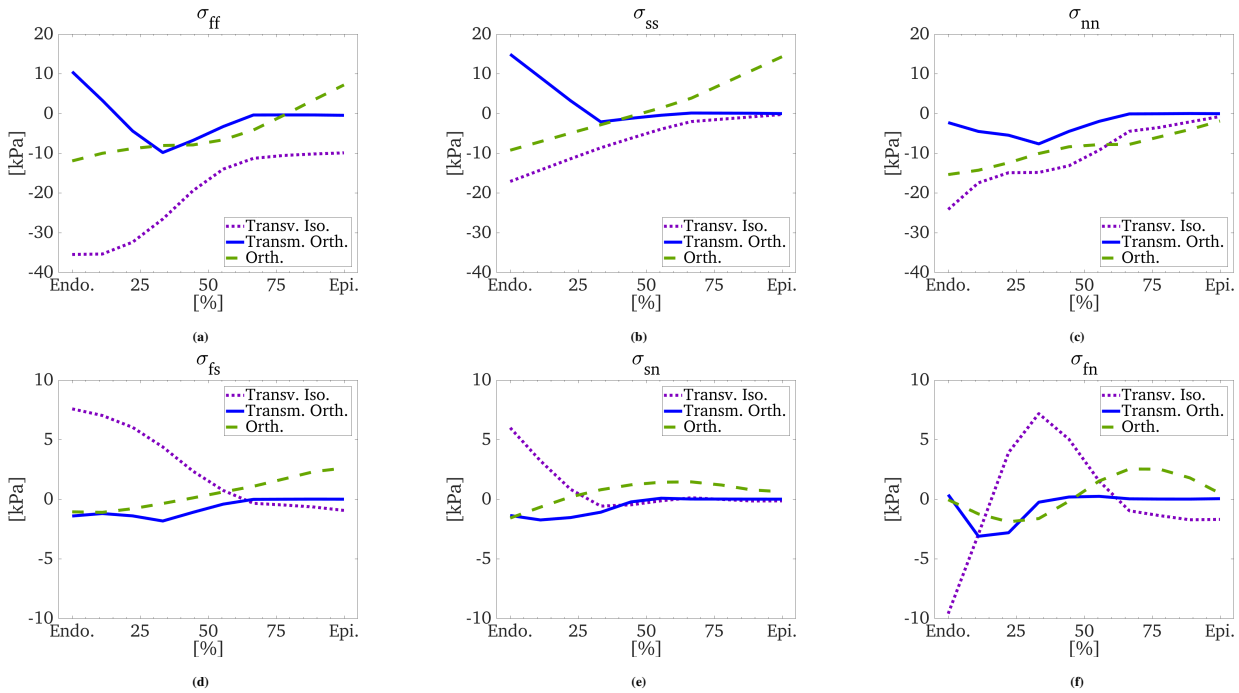

FIGURE 9 Systolic stresses at equatorial height with $p_v = 14$ kPa. The six independent components of the Cauchy stress tensor in material coordinates system (σ_{ff}, σ_{ss}, σ_{nn}, σ_{fs}, σ_{sn}, σ_{fn}) are plotted over a normalized transmural coordinate. The three lines represent stresses for the transversely isotropic (··), orthotropic (–) and transmurally heterogeneous orthotropic (-) activation models. The top line displays the axial stresses along fibers, sheets and normals. The bottom line displays the shear stresses.

Fig. 9 shows the stress state of the myocardium along the three orthotropic directions, **f**, **s**, and **n**. Axial and shear stresses have been evaluated at the equatorial region of the ventricle at the end of systolic phase when p_v reached 14 kPa. We notice in Fig. 9 a, 9 b and 9 c, that the heterogeneous orthotropic activation model yields a more uniform distribution of axial stresses, and therefore an overall lower stress state. This complies with the tendency of biological tissues to grow and remodel due to mechanical stimuli. A large variation in the stress distribution would lead to a growth in the regions subjected to greater loads and to a decrease of muscular tone in regions with smaller stresses. Since it is difficult, if not impossible, to measure the active stresses in the whole living myocardium, a homogeneity argument for the stresses can be used to interpret the results. Following this principle, the transversely isotropic activation model shows the largest transmural variation of the stresses, ranging from -35 to -15 kPa at the endocardium and from -10 to 0 kPa at the epicardium. Shear stresses also exhibits a large variation ranging from -10 to 7.5 kPa. Regarding the stresses, the orthotropic model and the transmurally heterogeneous orthotropic model have a similar behavior. The orthotropic model has slightly larger axial stresses σ_{ff}, σ_{ss}, σ_{nn} and a less uniform distribution in Ω_0. The stress computed using the transmurally heterogeneous orthotropic activation presented in this work are generally more uniformly distributed.

6 | CONCLUSIONS

In this work, we proposed a new model for the active description of the ventricular contraction accounting for transmural heterogeneity. Transmural heterogeneities in the myocardial strains have been revealed by experimental studies long ago[49]. In fact, the shortening deformation, orthogonal to the local fiber direction, has been shown to be larger than fiber shortening itself in the inner half of the ventricular wall. This fact suggests that some sort of rearrangment of the myocytes takes place during contraction[50,49]. Such rearrangement is at the basis of the devolopment of the orthotropic active strain formulation[20]. In fact, the hypothesis that ventricular wall thickening is the result of increased fiber cross-sections due to volume preserving fiber shortening contradicts local and global strain measurements[49]. Additionally, the ejection fractions that would be realized from such a mechanism would be too small. On the contrary, the orthotropic active strain formulation well captures the overall systolic wall thickening and the physiological ejection fraction: simple geometrical

assumptions link the fiber shortening with collagen inextensibility, thus resulting in an anisotropic multiscale description of the ventricular contraction. Nonetheless, the orthotropic active strain model as originally proposed in [20] cannot reproduce the transmural heterogeneities of systolic strains.

By numerically simulating the full cardiac cycle, we evaluated the wall strains and we compared the results with the experimental data in [49,47]. We have shown through our numerical results the limitation of the orthotropic model [20] in capturing the correct ventricular shortening and torsion. Similarly, we have shown the limitations of the transversely isotropic active strain model [19] in capturing the circumferential strains and in-plane rotations. Instead, our proposed active strain model gives a better description of shear strains. In particular, it captures more accurately than the other models the strains related to rotation and torsion (circumferential-radial and circumferential-longitudinal) which are indicators of cardiac performance and have been proven to be sensitive to the presence of many pathologies ([51,52,53,54,55,56]), while maintaining the ability to describe large wall thickening. For reference, we have also reported the numerical results of a study that used an active stress model [17]. The main limitation of the orthotropic active strain models is in the description of the longitudinal strain. In fact, the magnitude of this strain is larger than the measured one, although the transmurally heterogeneous orthotropic activation model improves the prediction of this strain. Indeed, the transmurally heterogeneous orthotropic activation model improves the prediction of circumferential strains and longitudinal strain of transversely isotropic and orthotropic activation models respectively, while capturing correctly shear strains related to in-plane rotation and ventricular torsion. The behavior of the strains in the proposed transmurally heterogenous orthotropic model is in qualitative agreement with the experimental data.

We have also evaluated and compared the transmural stress distributions for all active strain models under consideration. Both orthotropic activation models provide axial stresses lower than the transversely isotropic activation model and a more uniform transmural distribution of the shear stresses. This is due to the description of the complex micro-structure of the myocardium introduced by the orthotropic model, where the myocardial activation considers the interactions between myocytes and collagen sheets.

The effect of surrounding organs and tissues was modeled by means of a Robin boundary condition at epicardium. We performed a sensitivity analysis for the coefficient of the Robin boundary conditions used on the epicardial surface and we confirmed that,as previously reported [48], the pericardium plays an important role during diastole by enforcing myocardial stiffness. We used such boundary condition also for the systolic phase. Although we did not consider the influence of different boundary conditions on the systolic strains, we believe that those may play a major role in determining the actual epicardial strains. In general, the type of boundary conditions to use in ventricular cardiac models still remains an open question.

In conclusion transmural variations of the active contraction play a major role in determining systolic strains. The newly proposed transmurally heterogeneous orthotropic activation model describes more accurately than the other models ventricular contraction. Specifically, the proposed model provides more accurate strain distributions as shown by the validation against experimental measurements.

ACKNOWLEDGMENTS

The authors would like to thank Dr. E. Faggiano and Prof. D. Ambrosi for the precious support given at the beginning of this research. The authors would also like to thank Dr. S. Pezzuto and Dr. D. Bonomi for their help with the software and the mesh and the whole CMCS group at EPFL for all the stimulating discussions.

References

1. Quarteroni Alfio, Lassila Toni, Rossi Simone, Ruiz-Baier Ricardo. Integrated Heart-Coupling multiscale and multiphysics models for the simulation of the cardiac function. *Computer Methods in Applied Mechanics and Engineering.* 2017;314:345–407.

2. Yancy Clyde W, Jessup Mariell, Bozkurt Biykem, et al. 2013 ACCF/AHA guideline for the management of heart failure. *Circulation.* 2013;128(16):e240–e327.

3. Vigmond Edward J, Clements Clyde, McQueen David M, Peskin Charles S. Effect of bundle branch block on cardiac output: a whole heart simulation study. *Progress in biophysics and molecular biology.* 2008;97(2):520–542.

4. Sugiura Seiryo, Washio Takumi, Hatano Asuka, Okada Junichi, Watanabe Hiroshi, Hisada Toshiaki. Multi-scale simulations of cardiac electrophysiology and mechanics using the University of Tokyo heart simulator. *Progress in biophysics and molecular biology.* 2012;110(2):380–389.

5. Baillargeon Brian, Rebelo Nuno, Fox David D, Taylor Robert L, Kuhl Ellen. The living heart project: a robust and integrative simulator for human heart function. *European Journal of Mechanics-A/Solids.* 2014;48:38–47.

6. Crozier A, Augustin CM, Neic A, et al. Image-based personalization of cardiac anatomy for coupled electromechanical modeling. *Annals of biomedical engineering.* 2016;44(1):58–70.

7. Lee Jack, Cookson A, Roy Ishani, et al. Multiphysics computational modeling in CHeart. *SIAM Journal on Scientific Computing.* 2016;38(3):C150–C178.

8. McCulloch Andrew D. Systems Biophysics: Multiscale Biophysical Modeling of Organ Systems. *Biophysical journal.* 2016;110(5):1023.

9. Quarteroni A, Manzoni A, Vergara C. The cardiovascular system: Mathematical modelling, numerical algorithms and clinical applications. *Acta Numerica.* 2017;26:365–590.

10. Nordsletten D.A., Niederer S.A., Nash M.P., Hunter P.J., Smith N.P.. Coupling multi-physics models to cardiac mechanics. *Progress in Biophysics and Molecular Biology.* 2011;104(1âĂŞ3):77 - 88.

11. Ponnaluri AVS, Perotti LE, Ennis DB, Klug WS. A viscoactive constitutive modeling framework with variational updates for the myocardium. *Computer Methods in Applied Mechanics and Engineering.* 2017;314:85–101.

12. Eriksson TSE, Prassl AJ, Plank G, Holzapfel Gerhard A. Influence of myocardial fiber/sheet orientations on left ventricular mechanical contraction. *Mathematics and Mechanics of Solids.* 2013;18(6):592–606.

13. Holzapfel Gerhard A, Ogden Ray W. Constitutive modelling of passive myocardium: a structurally based framework for material characterization. *Philosophical Transactions of the Royal Society A: Mathematical, Physical and Engineering Sciences.* 2009;367(1902):3445–3475.

14. Bovendeerd PH, Kroon Wilco, Delhaas Tammo. Determinants of left ventricular shear strain.. *American Journal of Physiology. Heart and Circulatory Physiology.* 2009;297(3):H1058–68.

15. Bestel Julie, Clément Frédérique, Sorine Michel. A biomechanical model of muscle contraction. In: :1159–1161Springer; 2001.

16. Guccione Julius M, Costa Kevin D, McCulloch Andrew D. Finite element stress analysis of left ventricular mechanics in the beating dog heart. *Journal of Biomechanics.* 1995;28(10):1167–1177.

17. Haddad Seyyed M.H., Samani Abbas. A computational model of the left ventricle biomechanics using a composite material approach. *International Journal of Engineering Science.* 2017;111:61 - 73.

18. Ambrosi Davide, Arioli Gianni, Nobile Fabio, Quarteroni Alfio. Electromechanical coupling in cardiac dynamics: the active strain approach. *SIAM Journal on Applied Mathematics.* 2011;71(2):605–621.

19. Gjerald Sjur, Hake Johan, Pezzuto Simone, Sundnes Joakim, Wall Samuel T. Patient–specific parameter estimation for a transversely isotropic active strain model of left ventricular mechanics. In: :93–104Springer; 2014.

20. Rossi Simone, Lassila Toni, Ruiz-Baier Ricardo, Sequeira Adélia, Quarteroni Alfio. Thermodynamically consistent orthotropic activation model capturing ventricular systolic wall thickening in cardiac electromechanics. *European Journal of Mechanics-A/Solids.* 2014;48:129–142.

21. Göktepe Serdar, Menzel Andreas, Kuhl Ellen. The generalized Hill model: A kinematic approach towards active muscle contraction. *Journal of the Mechanics and Physics of Solids.* 2014;72:20–39.

22. Stålhand Jonas, Klarbring Anders, Holzapfel Gerhard A. A mechanochemical 3D continuum model for smooth muscle contraction under finite strains. *Journal of theoretical biology.* 2011;268(1):120–130.

23. Rademakers Frank E, Rogers Walter J, Guier William H, et al. Relation of regional cross-fiber shortening to wall thickening in the intact heart. Three-dimensional strain analysis by NMR tagging.. *Circulation.* 1994;89(3):1174–1182.

24. Rossi Simone, Ruiz-Baier Ricardo, Pavarino Luca F, Quarteroni Alfio. Orthotropic active strain models for the numerical simulation of cardiac biomechanics. *International Journal for Numerical Methods in Biomedical Engineering.* 2012;28(6-7):761–788.

25. Pezzuto Simone. Mechanics of the heart: constitutive issues and numerical experiments. PhD thesisPolitecnico di Milano2013.

26. Ciarlet Philippe G. *The finite element method for elliptic problems*. SIAM; 2002.

27. Simo JC, Taylor RL. Penalty function formulations for incompressible nonlinear elastostatics. *Computer Methods in Applied Mechanics and Engineering.* 1982;35(1):107–118.

28. Schröder Jörg, Viebahn Nils, Balzani Daniel, Wriggers Peter. A novel mixed finite element for finite anisotropic elasticity; the SKA-element Simplified Kinematics for Anisotropy. *Computer Methods in Applied Mechanics and Engineering.* 2016;310:475–494.

29. Costa K. D., Holmes J. W., Mcculloch A. D.. Modelling cardiac mechanical properties in three dimensions. *Philosophical Transactions of the Royal Society of London A: Mathematical, Physical and Engineering Sciences.* 2001;359(1783):1233–1250.

30. Fung Yuan-Cheng. Mathematical representation of the mechanical properties of the heart muscle. *Journal of Biomechanics.* 1970;3(4):381 - 404.

31. Legrice I. J., Hunter P. J., Smaill B. H.. Laminar structure of the heart: a mathematical model. *American Journal of Physiology - Heart and Circulatory Physiology.* 1997;272(5):H2466–H2476.

32. Holzapfel Gerhard A. *Nonlinear Solid Mechanics*. Wiley Chichester; 2000.

33. Flory PJ. Thermodynamic relations for high elastic materials. *Transactions of the Faraday Society.* 1961;57:829–838.

34. Sansour Carlo. On the physical assumptions underlying the volumetric-isochoric split and the case of anisotropy. *European Journal of Mechanics-A/Solids.* 2008;27(1):28–39.

35. Helfenstein J, Jabareen M, Mazza E, Govindjee S. On non-physical response in models for fiber-reinforced hyperelastic materials. *International Journal of Solids and Structures.* 2010;47(16):2056–2061.

36. Hartmann Stefan, Neff Patrizio. Polyconvexity of generalized polynomial-type hyperelastic strain energy functions for near-incompressibility. *International Journal of Solids and Structures.* 2003;40(11):2767–2791.

37. Simo Juan C, Taylor Robert L. Quasi-incompressible finite elasticity in principal stretches. Continuum basis and numerical algorithms. *Computer Methods in Applied Mechanics and Engineering.* 1991;85(3):273–310.

38. Boyett MR, Frampton JE, Kirby MS. The length, width and volume of isolated rat and ferret ventricular myocytes during twitch contractions and changes in osmotic strength. *Experimental Physiology.* 1991;76(2):259–270.

39. Quinn T Alexander, Kohl Peter. Combining wet and dry research: experience with model development for cardiac mechano-electric structure-function studies. *Cardiovascular Research.* 2013;97(4):601–611.

40. Wong Jonathan, Kuhl Ellen. Generating fibre orientation maps in human heart models using Poisson interpolation. *Computer Methods in Biomechanics and Biomedical Engineering*. 2014;17(11):1217–1226.

41. Geuzaine Christophe, Remacle Jean-François. Gmsh: A 3-D finite element mesh generator with built-in pre-and post-processing facilities. *International journal for numerical methods in engineering.* 2009;79(11):1309–1331.

42. Ben-Israel Adi. A Newton-Raphson method for the solution of systems of equations. *Journal of Mathematical Analysis and Applications.* 1966;15(2):243 - 252.

43. Quarteroni Alfio, Sacco Riccardo, Saleri Fausto. *Numerical mathematics*. Springer Science & Business Media; 2010.

44. Quarteroni Alfio, Valli Alberto. *Domain decomposition methods for partial differential equations*. No. CMCS-BOOK-2009-019Oxford University Press; 1999.

45. Tricerri Paolo, Dedè Luca, Gambaruto Alberto, Quarteroni Alfio, Sequeira Adélia. A numerical study of isotropic and anisotropic constitutive models with relevance to healthy and unhealthy cerebral arterial tissues. *International Journal of Engineering Science.* 2016;101:126–155.

46. Westerhof Nico, Lankhaar Jan-Willem, Westerhof Berend E.. The arterial Windkessel. *Medical & Biological Engineering & Computing.* 2009;47(2):131–141.

47. Omens Jeffrey H, May KAREN D, McCulloch Andrew D. Transmural distribution of three-dimensional strain in the isolated arrested canine left ventricle. *American Journal of Physiology-Heart and Circulatory Physiology.* 1991;261(3):H918–H928.

48. Glantz Stanton A, Misbach Gregory A, Moores William Y, et al. The pericardium substantially affects the left ventricular diastolic pressure-volume relationship in the dog.. *Circulation Research.* 1978;42(3):433–441.

49. Waldman Lewis K, Nosan David, Villarreal Francisco, Covell James W. Relation between transmural deformation and local myofiber direction in canine left ventricle.. *Circulation Research.* 1988;63(3):550–562.

50. Spotnitz Henry M, Spotnitz William D, Cottrell Thomas S, Spiro David, Sonnenblick Edmund H. Cellular basis for volume related wall thickness changes in the rat left ventricle. *Journal of molecular and cellular cardiology.* 1974;6(4):317–331.

51. Young Alistair A, Cowan Brett R. Evaluation of left ventricular torsion by cardiovascular magnetic resonance. *Journal of Cardiovascular magnetic resonance.* 2012;14(1):49.

52. Kanzaki Hideaki, Nakatani Satoshi, Yamada Naoaki, Urayama Shin-ichi, Miyatake Kunio, Kitakaze Masafumi. Impaired systolic torsion in dilated cardiomyopathy: reversal of apical rotation at mid-systole characterized with magnetic resonance tagging method. *Basic Research in Cardiology.* 2006;101(6):465–470.

53. Fonseca Carissa G, Dissanayake Ajith M, Doughty Robert N, et al. Three-dimensional assessment of left ventricular systolic strain in patients with type 2 diabetes mellitus, diastolic dysfunction, and normal ejection fraction. *The American journal of cardiology.* 2004;94(11):1391–1395.

54. Nagel Eike, Stuber Matthias, Burkhard Barbara, et al. Cardiac rotation and relaxation in patients with aortic valve stenosis. *European Heart Journal.* 2000;21(7):582–589.

55. Bertini Matteo, Delgado Victoria, Nucifora Gaetano, et al. Left ventricular rotational mechanics in patients with coronary artery disease: differences in subendocardial and subepicardial layers. *Heart.* 2010;96(21):1737–1743.

56. Lumens Joost, Delhaas Tammo, Arts Theo, Cowan Brett R, Young Alistair A. Impaired subendocardial contractile myofiber function in asymptomatic aged humans, as detected using MRI. *American Journal of Physiology-Heart and Circulatory Physiology.* 2006;291(4):H1573–H1579.

MOX Technical Reports, last issues

Dipartimento di Matematica
Politecnico di Milano, Via Bonardi 9 - 20133 Milano (Italy)

61/2017 Vadacca, L.; Colciago, C. M.; Micheletti, S.; Scotti, A.
Three-dimensional fault representation by interface and solid elements: effects of the anisotropy of the fault zone permeability on the timing of triggered earthquakes

60/2017 Bonaldi, F.; Di Pietro, D. A.; Geymonat, G.; Krasucki, F.
A Hybrid High-Order method for Kirchhoff-Love plate bending problems

59/2017 Grujic, O.; Menafoglio, A.; Guang, Y.; Caers, J.
Cokriging for multivariate Hilbert space valued random fields. Application to multifidelity computer code emulation

58/2017 Landajuela, M.; Vergara, C.; Gerbi, A.; Dede', L.; Formaggia, L.; Quarteroni, A.
Numerical approximation of the electromechanical coupling in the left ventricle with inclusion of the Purkinje network

57/2017 Ballarin, F.; D'Amario, A.; Perotto, S.; Rozza, G.
A POD-Selective Inverse Distance Weighting method for fast parametrized shape morphing

56/2017 Alberti, G. S.; Santacesaria, M.
Infinite dimensional compressed sensing from anisotropic measurements

53/2017 Bertagna, L.; Deparis, S.;Formaggia, L.; Forti, D.; Veneziani A.
The LifeV library: engineering mathematics beyond the proof of concept

54/2017 Dede', L; Quarteroni, A.
Isogeometric Analysis of a Phase Field Model for Darcy Flows with Discontinuous Data

55/2017 Agosti, A.; Cattaneo, C.; Giverso, C.; Ambrosi, D.; Ciarletta, P.
A computational platform for the personalized clinical treatment of glioblastoma multiforme

52/2017 Beretta, E.; Ratti, L.; Verani, M.
A phase-field approach for the interface reconstruction in a nonlinear elliptic problem arising from cardiac electrophysiology